Evidence and stability field of fcc superionic water ice using static compression

Gunnar Weck, Jean-Antoine Queyroux, Sandra Ninet, Frédéric Datchi, Mohamed Mezouar, Paul Loubeyre

Evidence and stability field of fcc-superionic water ice using static compression

Gunnar Weck,[1,2,*] Jean-Antoine Queyroux,[1] Sandra Ninet,[3]
Frédéric Datchi,[3] Mohamed Mezouar,[4] and Paul Loubeyre[1,2]

[1] *CEA, DAM, DIF, F-91297 Arpajon, France*
[2] *Univ Paris Saclay, Lab Matiere Condit Extremes, CEA, F-91680 Bruyeres Le Chatel, France*
[3] *Institut de Minéralogie, de Physique des Matériaux et de Cosmochimie (IMPMC), Sorbonne Université, CNRS UMR 7590, IRD UMR 206, MNHN, 4 place Jussieu, F-75005 Paris, France*
[4] *European Synchrotron Radiation Facility, Boîte Postale 220, 38043 Grenoble, France*

(Dated: March 6, 2023)

Structural transformation of hot dense water ice is investigated by combining synchrotron x-ray diffraction and a laser-heating diamond anvil cell above 25 GPa. A transition from the body-centered-cubic (bcc) to face-centered-cubic (fcc) oxygen atoms sublattices is observed from 57 GPa and 1500 K to 166 GPa and 2500 K. That is the structural signature of the transition to fcc-superionic (fcc-SI) ice. The sign of the density discontinuity at the transition is obtained and a phase diagram is disclosed, showing an extended fcc-SI stability field. Present data also constrain the stability field of the bcc-superionic (bcc-SI) ice up to 100 GPa at least. The current understanding of warm dense water ice based on *ab initio* simulations is discussed in the light of present data.

PACS numbers: Valid PACS appear here

Introduction. The polymorphism of ice under pressure is extraordinarily rich, with a remarkable diversity of oxygen atoms sublattices up to about 3 GPa [1]. Above this pressure, the structures are essentially built on a body-centered cubic (bcc) oxygen sublattice, the first one being ice VII. By transiting to ice X, about 60 GPa, H_2O ice reaches a symmetric H-bonding regime in which individual H_2O molecules are no longer discernible [2–4]. Instead, the hydrogen atoms are located midway between nearest neighbor oxygen atoms. Ice X is an ionic solid which has been measured stable up to at least 170 GPa at 300 K [5]. Upon heating, the hydrogen bond weakens and ice VII is expected to transform into a superionic (SI) phase in which a rigid oxygen sublattice coexists with mobile protons [6].

There is a great current interest in studying the phases and the properties of warm dense ice. Those are needed to model the planetary interiors of Uranus, Neptune, and other ice giant exoplanets being discovered [7]. Under planetary interior conditions, part of the ice layer is projected to be in a superionic (SI) state. The protonic conductivity associated to SI ice should have implications for the magnetic field of the Neptune-like planets [8]. SI ice was first predicted to have a fcc oxygen sublattice [9]. Then, early ab-initio simulations considered SI ice with a bcc oxygen sublattice, as a high temperature analogue of ice X [10]. Many ab-initio studies have now been devoted to disclose the phase diagram of SI ice [10–14]. Various structures are proposed to be stable below 1 TPa with bcc, fcc and other close-packed (cp) oxygen sublattices. The stability field and the properties of these various forms of superionic ice is currently debated.

Several experimental works have aimed at finding evidence for the existence of SI ice. Difficulties arise because it is challenging to confine reactive hot-dense H_2O and because of the weak x-ray scattering power of the H_2O sample. Several static compression studies have claimed indirect evidences of bcc-SI ice, mainly by observing a kink on the melting curve. However, there is a lack of consensus among these various melting line determinations [15–18]. A clear evidence for superionic conduction in water ice was obtained by shock wave optical properties measurements [19]. Structural changes associated to the transition to the SI state were then measured by x-ray diffraction (XRD). First, multiple-shocks dynamic compression of ice combined with XRD reported evidence of the fcc-SI phase, labeled ice XVIII, above 160 GPa [20]. However, coupling XRD to dynamic compression is challenging and only one Bragg reflection could be followed, ascribed at low pressure to the bcc (110) and after a +2.7% d-spacing discontinuity to the fcc (111). Subsequently, clear evidence of the transition from bcc to bcc-SI ice could be observed close to the melting line above 14.6 GPa and 850 K, associated to a volume discontinuity of +2.2(1)%, by performing synchrotron x-ray diffraction measurements in the resistively-heated diamond anvil cell [21]. The aim of the present study is: i) to remove any ambiguities in that first claim of the observation of fcc-SI by obtaining a more complete fcc structural signature and by ruling out possible metastability effects associated to dynamic compression; ii) to disclose the phase diagram of superionic ice by covering the phase space between the observation of bcc-SI up to 45 GPa and that of fcc-SI above 160 GPa. A very recent static compression study [22], published during the review of the present work, has confirmed the existence of both bcc-SI and fcc-SI ices but the reported fcc-SI stability field is different from the one disclosed from dynamic compression. In contrast here below, the present results are consistent with both dynamic compression data [20]

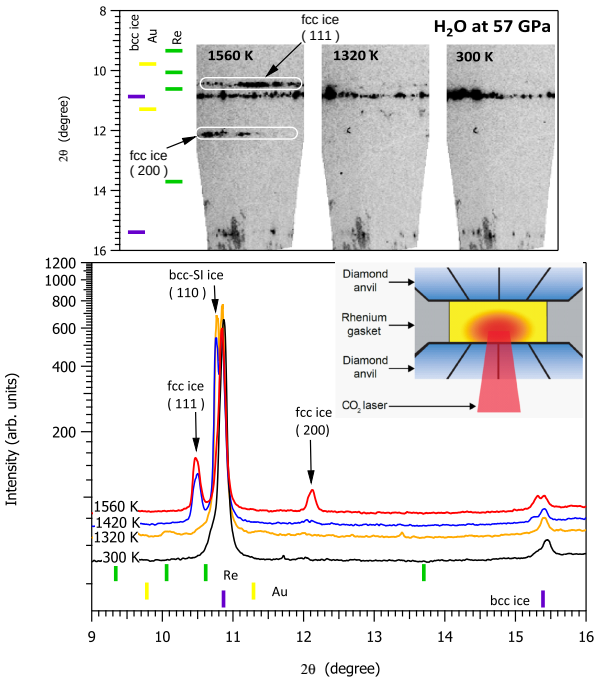

FIG. 1. Typical XRD patterns associated to the CO_2 laser heating configuration, as obtained for the heating run at 57 GPa. a) Section of the X-ray diffraction 2D images collected at 57 GPa-1560 K (left), -1320 K (middle) and -300 K (right), respectively above and below the bcc-fcc transition and after the heating cycle. The Bragg peaks of bcc and fcc phases of ice are tagged. b) XRD patterns. The intensity of the diffraction peaks is displayed in a log scale. The spectra have been shifted vertically and the peaks coming from the diamond anvils have been masked for clarity. The double peak structure of bcc 110 at 1320 K is indicative of the transition to bcc-SI. The inset shows a sketch of a cross-sectional view of the H_2O sample cavity under direct CO_2 laser heating, with the hot ice volume in red.

and the most recent theoretical calculations [14].

Experimental approach. Experiments were performed on water samples compressed in membrane diamond anvil cells. The complete experimental methods are given in the Supplemental Material file (SM)[23]. Two different configurations were used for laser-heating the H_2O sample. First, by using a CO_2 laser which is directly absorbed by the H_2O sample. Doing so, a hot H_2O volume can be embedded within the cold H_2O sample, hence providing a good confinement of this reactive sample. This approach recently enabled us to measure the melting line of H_2O using XRD up to 45 GPa [21]. In the present work, such measurements were performed on two samples up to 62 GPa. At higher pressures, that approach becomes inoperative possibly because of a reduced absorption of the 10.6 µm radiation by the H_2O sample. Therefore, for pressures of about 70 GPa and above, an indirect heating of H_2O sample was implemented, based on the use of a boron-doped diamond absorber (C:B) disk, similarly to our previous works on the melting curve of N_2 and Au [24, 25]. The drawing of the sample configuration is shown in Fig. 2b. In that case, a YLF laser is used to effectively heat the (C:B) disk, which is FIB-machined in a cupped form. The typical dimension of the cup heater, hence of the hot dense ice volume probed, was 12 µm in diameter and 5-6 µm in depth. The C:B disk was placed at the center of a FIB-machined pit on one diamond anvil culet. Two samples successfully reached the H_2O fcc-SI phase, with heating ramps around 100 GPa and 160 GPa, respectively.

Angular dispersive XRD experiments were conducted at the ID27 beamline of the European Synchrotron Radiation Facility (ESRF, Grenoble, France). The 0.3738 Å x-ray beam was focused to a 3×3 μm^2 spot and the diffraction signal was collected on a 165-mm diameter MAR CCD detector. A multi-channel collimator (MCC) was used in the CO_2 laser heating run [26]. This device significantly reduces the Compton contribution of the diamond anvils, resulting in a flat background over which the sample signal is clearly seen, as illustrated in Fig. 1. However, the use of a MCC significantly increases the acquisition time since it also filters out part of the H_2O sample signal. The MCC was not used in the YLF laser heating configuration. The typical XRD patterns obtained in that case are shown in Fig. 2b. The diffraction peaks of ice and of the C:B disk are clearly observed above the Compton contribution of the diamond anvils. A detailed description of the laser-heating setup is given elsewhere [27, 28].

Temperature was estimated from the sample thermal emission collected over 550–950 nm from both sides of the LH-DAC and fitted with the Planck formula within a grey body approximation [29]. Temperature could be measured only above 1000 K and temperature uncertainty was estimated to be less than ±300 K (see section IB of SM). We note that in both heating configurations, a large temperature gradient is present over the sample thickness, as evidenced by the presence of both cold (∼ 300 K) and hot diffraction peaks in the XRD patterns. As shown in Refs. [21, 30], even in the presence of such large temperature gradients, the effective pyrometric temperature corresponds, within 5 %, to the peak temperature.

Sample pressure was estimated from the measured volumes of the hot diamond absorber or cold gold liner [31, 32], depending on the heating configuration (see section IA of SM). The pressure uncertainty is estimated about ±4 GPa in the 100 GPa range [24].

Structural evidence of bcc-SI and fcc-SI phases. For all the runs, x-ray diffraction patterns were collected by keeping the force on the DAC piston constant and by gradually increasing and stabilizing the temperature in steps so to enable XRD and pyrometry measurements. Doing so, the pressure measured along the heating ramps remained quasi constant. The initial ramp pressure ranged from 27 to 170 GPa. A XRD pattern was

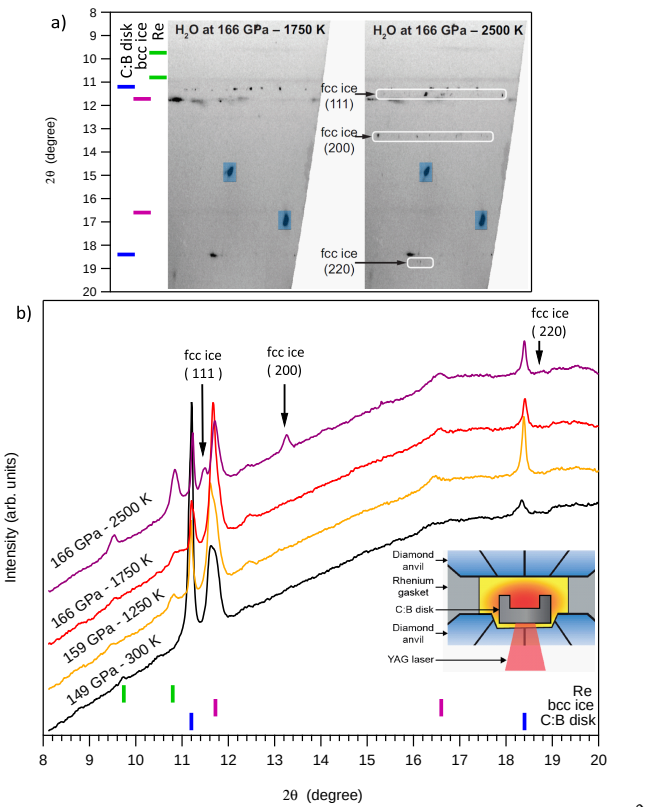

FIG. 2. Typical XRD patterns associated to the YLF laser heating configuration, as obtained for the heating run at 166 GPa. a) Section of the XRD 2D images collected at 166 GPa-1750 K (left) and 166 GPa-2500 K (right) collected just before and after the bcc-fcc transition. Tick marks indicate the Bragg peak positions of the compounds present in the sample chamber. The diamond anvil diffraction peaks are tagged in blue and masked. b) Integrated XRD patterns of water measured at several temperatures around 166 GPa. The spectra have been shifted vertically for clarity. The inset shows a sketch of a cross-sectional view of the H_2O sample cavity with the C:B absorber disk positioned in a pit made on the anvil tip.

also measured at ambient temperature after each heating ramp so to check for the chemical integrity of the H_2O sample.

Using CO_2 laser heating, the transition from the insulating bcc ice VII or ice VII' to the bcc-SI ice [6, 21] could be clearly observed at 27, 33, 40 and 57 GPa, as illustrated in Fig. 1 (see also supplementary part II.A and Figs. S3 and S4).The discontinuous density drop at the bcc to bcc-SI transition was revealed by the appearance of novel bcc diffraction peaks well separated from those of ice VII/VII' at 300K. Before the transition, only an asymmetric broadening of the diffraction peaks towards low angle is observed, associated to the contribution of the hot ice VII/VII' convoluted with that at 300 K. In the higher-pressure runs performed under YLF laser heating, it is difficult to ascertain the existence of a bcc-SI phase from the diffraction patterns. A significant broadening (see Fig. 2) of the diffraction peaks due to deviatoric stress is observed which also becomes asymmetric at high temperature due to the temperature gradient.

The transition from bcc to fcc ice could be clearly observed for both heating configurations. Under CO_2 laser heating, with the appearance of the (111) and (200) reflections around 1400(150) K and 1600(150) K at 57 GPa and 62 GPa respectively, as shown in Fig 1 (and Fig. S4). Note that higher-angle reflections cannot be accessed due to the angular aperture limitation of the MCC. Under YLF laser heating, the MCC was not used and the (220) reflection could be detected in addition to (111) and (200) ones above 1850(200) K at 95 GPa (see Fig. S5) and around 2500 K at 166 GPa (see Fig. 2).

It should be noted that the bcc phase is still observed on XRD patterns collected at temperatures greater than the bcc-fcc transition temperature, because of the temperature gradient within the sample. However, above the transition temperature, the volume-per-molecule of bcc ice does not vary from its value at the bcc-fcc transition point, whereas the one of fcc shows a thermal expansion with increasing temperature, (as illustrated in Fig. S6 for the 57 GPa heating ramp). The densities of the bcc and fcc phases in equilibrium at the transition point are thus estimated at the lowest temperature where the fcc phase is detected. For $P < 60$ GPa, fcc is in equilibrium with bcc-SI which is well identified. For $P > 60$ GPa, the bcc-SI is not clearly observed, so the density of the "hot" bcc ice is deduced from the deconvolution of the bcc reflections into two contributions, one coming from the heated sample volume and the other from the sample part in contact with the anvils which remains "cold" (i.e. at 300 K). As seen in Fig. 3, the fcc phase ice is observed to have a slightly higher density than the bcc one for all the characterized transition points, yet the value of this density difference is within uncertainties.

EOS data. The measured densities of ice at various P-T conditions are plotted in Fig. 3, together with previous data from static [5, 21, 33–35] and dynamic [20] compression experiments. They are compared to ab-initio calculations using the Perdew-Burke-Ernzerhof (PBE) exchange-correlation (XC) functional for the insulating bcc (phases VII/VII') [36], and for the SI bcc and SI fcc ices [13]. Below 60 GPa, experimental and PBE densities of the insulating bcc ice are in very good agreement. For P>60 GPa, the scatter in the 300 K experimental data significantly increases and the densities deviate from the PBE curve. These scatter and deviation could originate from deviatoric stress and pressure gradients in the ice sample, as observed in the present experiments. Indeed, our 300 K data measured after laser heating – which is known to, at least partially, release deviatoric stress – fall closer to the PBE curve calculated for perfect hydrostatic conditions. Furthermore, PBE densities agree very well with the high-T (400-1000 K) resistive heating DAC data

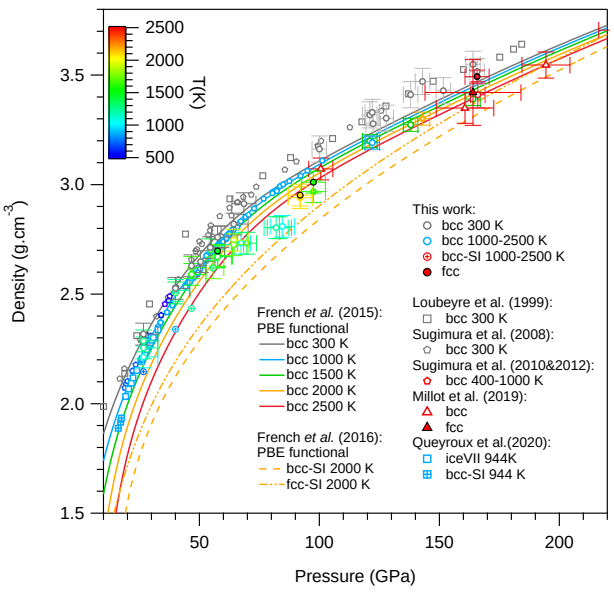

FIG. 3. Comparison between calculated and measured densities versus pressure for bcc, bcc-SI and fcc-SI ice. The color scale corresponds to the temperature of the hot spot measured by spectroradiometry. The symbols indicate experimental data of present work and previous works [5, 21, 33–35]. Pressure values for Ref. [5] were corrected to account for the updated ruby scale [37]. Full, dotted and dashes lines indicate DFT-PBE calculations for bcc, bcc-SI and fcc-SI [13, 36], respectively.

for the insulating ice VII/VII' [21, 34, 35] which should be less affected by deviatoric stresses.

The density of bcc-SI, measured in Ref. [21] and here to 60 GPa, is significantly lower than that of the insulating ice VII/VII'. The difference is seen to increase with pressure, as predicted by calculations [13, 36]. Above 60 GPa, the diffraction peaks of the insulating and SI bcc phases overlap but the densities extracted from the "hot" component are in closer agreement with the extrapolation of the lower-P data for bcc SI than for insulating ice up to 100 GPa. This suggests that the stability field of bcc SI extends to at least 100 GPa. By contrast, the densities above 120 GPa and up to 2000 K fall close to the PBE values for the bcc phases, which seems to indicate that, above 120 GPa, bcc ice remains insulating up to the transition to the fcc-SI.

Phase diagram. The measured data points are positioned on the H_2O phase diagram in Fig. 4, with symbols differentiating whether only bcc, or bcc and fcc phases are observed. The boundary line between the bcc and fcc-SI phases is thereof constrained between 50 and 166 GPa and it is seen to have a positive slope up to at least 120 GPa. Since the measured volume of fcc-SI is less than the one of bcc at all transition pressures, the Clapeyron relation implies that, up to 120 GPa at least, the entropy of fcc-SI should be less than the bcc one. That is only possible if the bcc phase at the transition is also superionic. This is consistent with observations made above based on XRD and density data. At 160 GPa, our measured densities suggest the bcc phase to be insulating at the transition. Since we expect an increase in entropy going from the insulating bcc to fcc-SI, the Clapeyron slope should then be negative at this pressure. This would imply a maximum transition temperature on the bcc-fcc transition line of about 2300 ($\pm$300) K, located between 120 and 160 GPa, as illustrated in Fig. 4. We also note that present static data connect well with those obtained by dynamic compression [20]. This indicates that the latter are not affected by kinetic nor deviatoric stress effects.

The bcc-fcc transition lines obtained by various DFT calculations [11–14], all using the PBE functional, are shown in Fig. 4. Among these largely scattered predictions, it can be seen that the most recent work by Cheng et al [14] is in nice agreement with the experimental phase diagram disclosed by the present static and previous dynamic compression studies [20]. Ref. [14] used a machine learning potential trained on DFT-PBE simulations to run large scale simulations with advanced free energy methods to carefully estimate the entropy which appears crucial for a correct location of the boundary lines. Furthermore, these calculations predict a region of stability for the bcc-SI phase before the transition to fcc-SI up to about 120 GPa, which is consistent with present experimental data.

The phase diagram obtained by a recent experimental work [22] is compared with our results in Fig. S7. Both studies used the same techniques, i.e. laser heating in a DAC coupled with X-ray diffraction, but their findings show significant differences, notably in the stability domains of bcc-SI and fcc-SI ices. Indeed, (1) the fcc-SI phase appears for $P > 29$ GPa in Ref. [22], while both Ref. [21] and the present work do not find evidence of it below 45 GPa; (2) the transition temperature between the bcc and fcc-SI phases increases much more rapidly in Ref. [22] than found both in Ref. [20] and here, the difference reaching $\sim$1500 K at 150 GPa. Such a discrepancy could originate from the difficulties in measuring the sample temperature and in detecting the appearance of the phases due to temperature gradients and weak x-ray scattering power of ice.

Conclusion. The present structural data, collected with two distinct laser heating configurations, provide a clear observation of the transitions from bcc to bcc-SI and to fcc-SI phases in water ice. A novel phase diagram is disclosed, composed of insulating bcc ice VII/VI'/X at low T, bcc-SI ice from 14 GPa up to at least 120 GPa for T in the range 850-2000 K, and of fcc-SI ice above $\sim$50 GPa and $\sim$1400 K. The present findings agree very well with previous dynamic compression experiments and theoretical calculations based on advanced simulations methods.

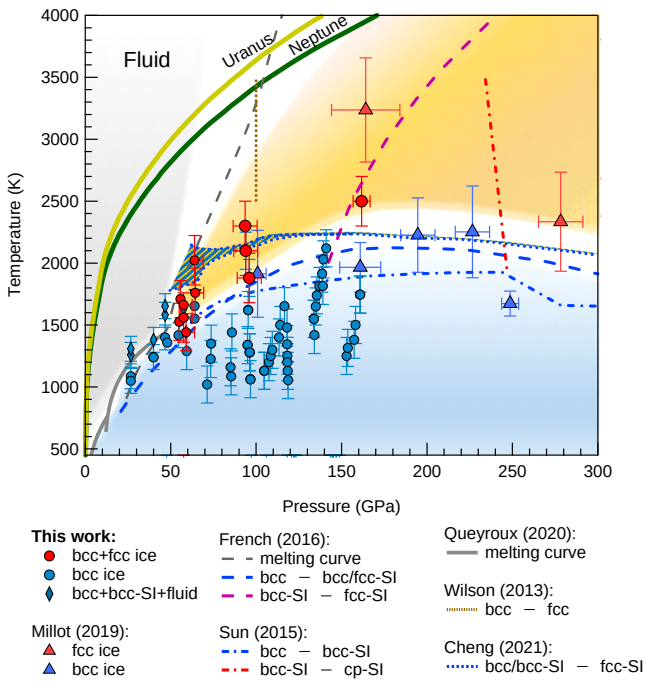

FIG. 4. Phase diagram of dense H_2O. The various colored domains correspond to the stability fields of: in grey, the molecular fluid; in blue, the bcc ices (ice VII, VII', X and bcc-SI); in yellow, the fcc-SI. The white zones represent the uncertainties on the transition lines. Blue circles represent the points where only the bcc phase was observed. The blue diamonds are the data where both bcc-SI and the fluid were observed. The red circles are the data points where the diffraction signal of fcc-SI was observed. The blue and red triangles correspond to bcc and fcc-SI data obtained under dynamic compression in Ref. [20]. The grey lines represent the experimental [21] (plain line) and theoretical [7] (dashed line) melting curves. The Uranus and Neptune isentropes [7] are represented as the yellow and green lines, respectively. The boundary lines between bcc and fcc-SI H_2O as calculated in various works [11–14] are drawn with different line-styles.

We acknowledge the European Synchrotron Radiation Facility for the provision of beam time under the proposals HC-3952, and financial support from the Agence Nationale de la Recherche under Grant No. ANR-13-BS04-0015 (MOFLEX) and No. ANR 15-CE30-0008-01 (SUPER-ICES). GW and JAQ have contributed equally to this work.

* gunnar.weck@cea.fr

[1] T. Bartels-Rausch, V. Bergeron, J. H. E. Cartwright, R. Escribano, J. L. Finney, H. Grothe, P. J. Gutiérrez, J. Haapala, W. F. Kuhs, J. B. C. Pettersson, et al., Rev. Mod. Phys. **84**, 885 (2012).
[2] W. B. Holzapfel, The Journal of Chemical Physics **56**, 712 (1972), ISSN 00219606.
[3] M. Benoit, D. Marx, and M. Parrinello, Nature **392**, 258 (1998), ISSN 0028-0836.
[4] J. M. Brown and B. Journaux, Minerals **10**, 92 (2020).
[5] P. Loubeyre, R. LeToullec, E. Wolanin, M. Hanfland, and D. Hausermann, Nature **397**, 503 (1999), ISSN 00280836.
[6] J.-A. Hernandez and R. Caracas, Phys. Rev. Lett. **117**, 135503 (2016).
[7] R. Redmer, T. R. Mattsson, N. Nettelmann, and M. French, Icarus **211**, 798 (2011), ISSN 0019-1035.
[8] K. M. Soderlund and S. Stanley, Philosophical Transactions of the Royal Society A: Mathematical, Physical and Engineering Sciences **378**, 20190479 (2020).
[9] P. Demontis, R. LeSar, and M. L. Klein, Phys. Rev. Lett. **60**, 2284 (1988).
[10] C. Cavazzoni, G. L. Chiarotti, S. Scandolo, E. Tosatti, M. Bernasconi, and M. Parrinello, Science **283**, 44 (1999).
[11] H. F. Wilson, M. L. Wong, and B. Militzer, Phys. Rev. Lett. **110**, 151102 (2013), ISSN 00319007.
[12] J. Sun, B. K. Clark, S. Torquato, and R. Car, Nat. Commun. **6**, 8156 (2015), ISSN 20411723.
[13] M. French, M. P. Desjarlais, and R. Redmer, Phys. Rev. E **93**, 022140 (2016).
[14] B. Cheng, M. Bethkenhagen, C. J. Pickard, and S. Hamel, Nature Physics pp. 1228–â€“1232 (2021).
[15] B. Schwager, L. Chudinovskikh, A. G. Gavriliuk, and R. Boehler, J. Phys.: Condens. Matter **16**, S1177 (2004).
[16] A. F. Goncharov, N. Goldman, L. E. Fried, J. C. Crowhurst, I.-F. Kuo, C. J. Mundy, and J. M. Zaug, Phys. Rev. Lett. **94**, 125508 (2005), ISSN 0031-9007.
[17] T. Kimura, Y. Kuwayama, and T. Yagi, J. Chem. Phys. **140**, 074501 (2014).
[18] M. Ahart, A. Karandikar, S. Gramsch, R. Boehler, and R. J. Hemley, High Pressure Res. **34**, 327 (2014).
[19] M. Millot, S. Hamel, J. R. Rygg, P. M. Celliers, G. W. Collins, F. Coppari, D. E. Fratanduono, R. Jeanloz, D. C. Swift, and J. H. Eggert, Nature Physics **14**, 297 (2018).
[20] M. Millot, F. Coppari, J. R. Rygg, A. Correa Barrios, S. Hamel, D. C. Swift, and J. H. Eggert, Nature **569**, 251 (2019), ISSN 0028-0836.
[21] J.-A. Queyroux, J.-A. Hernandez, G. Weck, S. Ninet, T. Plisson, S. Klotz, G. Garbarino, N. Guignot, M. Mezouar, M. Hanfland, et al., Phys. Rev. Lett. **125**, 195501 (2020).
[22] V. B. Prakapenka, N. Holtgrewe, S. S. Lobanov, and A. F. Goncharov, Nature Physics **17**, 1233 (2021).
[23] See Supplemental Material at [url] for details on the experimental methods, supplemental Figs. S1-S7, which includes Refs.[38–44].
[24] G. Weck, F. Datchi, G. Garbarino, S. Ninet, J.-A. Queyroux, T. Plisson, M. Mezouar, and P. Loubeyre, Phys. Rev. Lett. **119**, 235701 (2017).
[25] G. Weck, V. Recoules, J.-A. Queyroux, F. Datchi, J. Bouchet, S. Ninet, G. Garbarino, M. Mezouar, and P. Loubeyre, Phys. Rev. B **101**, 014106 (2020).
[26] G. Weck, G. Garbarino, S. Ninet, D. K. Spaulding, F. Datchi, P. Loubeyre, and M. Mezouar, Review of Scientific Instruments **84**, 63901 (2013).
[27] S. Petitgirard, A. Salamat, P. Beck, G. Weck, and P. Bouvier, J. Synchrotron Rad. **21**, 89 (2014).
[28] M. Mezouar, R. Giampaoli, G. Garbarino, I. Kantor, A. Dewaele, G. Weck, S. Boccato, V. Svitlyk, A. D. Rosa, R. Torchio, et al., High Pressure Res. **37**, 170 (2017), ISSN 0895-7959.

[29] L. Benedetti and P. Loubeyre, High Pressure Res. **24**, 423 (2004), ISSN 0895-7959.
[30] L. R. Benedetti, N. Guignot, and D. L. Farber, Journal of Applied Physics **101**, 13109 (2007), ISSN 00218979.
[31] P. I. Dorogokupets and A. Dewaele, High Pressure Research **27**, 431 (2007), ISSN 0895-7959.
[32] K. Takemura and A. Dewaele, Physical review B **78**, 104119 (2008).
[33] E. Sugimura, T. Iitaka, K. Hirose, K. Kawamura, N. Sata, and Y. Ohishi, Phys. Rev. B **77**, 214103 (2008).
[34] E. Sugimura, T. Komabayashi, K. Hirose, N. Sata, Y. Ohishi, and L. S. Dubrovinsky, Phys. Rev. B **82**, 134103 (2010).
[35] E. Sugimura, T. Komabayashi, K. Ohta, K. Hirose, Y. Ohishi, and L. S. Dubrovinsky, J. Chem. Phys. **137**, 194505 (2012).
[36] M. French and R. Redmer, Phys. Rev. B **91**, 014308 (2015), ISSN 1550235X.
[37] G. Shen, Y. Wang, A. Dewaele, C. Wu, D. E. Fratanduono, J. Eggert, S. Klotz, K. F. Dziubek, P. Loubeyre, O. V. Fatâ€™yanov, et al., High Pressure Research **40**, 299 (2020).
[38] R. Boehler and K. De Hantsetters, High Pressure Research **24**, 391 (2004), ISSN 08957959.
[39] F. Datchi, B. Mallick, A. Salamat, and S. Ninet, Physical Review Letters **108**, 125701 (2012).
[40] P. Vinet, J. Ferrante, J. Smith, and J. Rose, Journal of Physics C: Solid State Physics **19**, L467 (1986).
[41] J. A. Queyroux, S. Ninet, G. Weck, G. Garbarino, T. Plisson, M. Mezouar, and F. Datchi, Physical Review B **99**, 134107 (2019), ISSN 24699969.
[42] C. Prescher and V. B. Prakapenka, High Pressure Research **7959**, 223 (2015), ISSN 0895-7959.
[43] M. Mezouar, P. Faure, W. Crichton, N. Rambert, B. Sitaud, S. Bauchau, and G. Blattmann, Review of Scientific Instruments **73**, 3570 (2002), ISSN 00346748.
[44] G. Morard, M. Mezouar, S. Bauchau, M. Álvarez-Murga, J.-L. Hodeau, and G. Garbarino, The Review of scientific instruments **82**, 23904 (2011), ISSN 1089-7623.